18. Ferré S, Fuxe K, von Euler G, Johansson B, Fredholm BB. Adenosine-dopamine interactions in the brain. *Neuroscience* 1992;51:501–512.
19. Kirk IP, Richardson PJ. Adenosine A_{2a} receptor-mediated modulation of striatal [^{3}H]GABA and [^{3}H]acetylcholine release. *J Neurochem* 1994;62:960–966.
20. Kurokawa M, Koga K, Kase H, Nakamura J, Kuwana Y. Adenosine A_{2a} receptor-mediated modulation of striatal acetylcholine release in vivo. *J Neurochem* 1996;66:1882–1888.
21. Ishiwata K, Furuta R, Shimada J, et al. Synthesis and preliminary evaluation of [^{11}C]KF15372, a selective adenosine A_1 antagonist. *Appl Radiat Isot* 1995;46:1009–1013.
22. Furuta R, Ishiwata K, Kiyosawa M, et al. Carbon-11-labeled KF15372: a potential central nervous system adenosine A_1 recepter ligand. *J Nucl Med* 1996;37:1203–1207.
23. Noguchi J, Ishiwata K, Riko Furuta R, et al. Evaluation of carbon-11-labeled KF15372 and its ethyl and methyl derivatives as a potential CNS adenosine A_1 receptor ligand. *Nucl Med Biol* 1997;24:53–59.
24. Ishiwata K, Noguchi N, Toyama H, et al. Synthesis and preliminary evaluation of [^{11}C]KF17837, a selective adenosine A_{2A} antagonist. *Appl Radiat Isot* 1996;47:507–511.
25. Nonaka H, Mori A, Ichimura M, et al. Binding of [^{3}H]KF17837S, a selective adenosine A_2 receptor antagonist, to rat brain membranes. *Mol Pharmcol* 1994;46:817–822.
26. Nonaka Y, Shimada J, Nonaka H, et al. Photoisomerization of a potent and selective adenosine A_2 antagonist, (E)-1,3-dipropyl-8-(3,4-dimethoxystyryl)-7-methylxanthine. *J Med Chem* 1993;36:3731–3733.
27. Jacobson KA, Nikodijevic O, Padgett WL, Gallo-Rodriguez C, Maillard M, Daly JW.

28. Jacobson KA, Gallo-Rodriguez C, Melman N, et al. Structure-activity relationships of 8-styrylxanthines as A_2-selective adenosine antagonists. *J Med Chem* 1993;36:1333–1342.
29. Daly JW, Padgett WL, Shamim MT. Analogues of caffeine and theophylline: effect of structural alterations on affinity at adenosine receptors. *J Med Chem* 1986;29:1305–1308.
30. Poucher SM, Keddie JR, Singh P, et al. The in vitro pharmacology of ZM 241385, a potent, non-xanthine, A_{2a} selective adenosine receptor antagonist. *Br J Pharmacol* 1995;115:1096–1102.
31. Zocchi C, Ongini E, Conti A, et al. The non-xanthine heterocyclic compound SCH 58261 is a new potent and selective A_{2a} adenosine receptor antagonist. *J Pharmacol Exp Ther* 1996;276:398–404.
32. Shimada J, Suzuki F, Nonaka H, Ishii A. 8-Polycycloalkyl-1,3-dispropylxanthines as potent and selective antagonists for A_1-adenosine receptors. *J Med Chem* 1992;35:924–930.
33. Watanabe M, Uchida H, Okada H, et al. A high resolution PET for animal studies. *IEEE Trans Med Imag* 1992;11:577–580.
34. Sakiyama Y, Ishiwata K, Ishii K, et al. Evaluation of the brain uptake properties of [1-^{11}C]labeled hexanoate in anesthetoized cats by mean of positron emission tomography. *Ann Nucl Med* 1996;10:361–366.
35. Liang BT, Haltiwanger B. Adenosine A_{2a} and A_{2b} receptors in cultured fetal chick heart cells. High- and low-affinity coupling to stimulation of myocyte contractility amd cAMP accumulation. *Circ Res* 1995;76:242–251.

8-(3-Chlorostyryl)caffeine (CSC) is a selective A_2-adenosine antagonist in vitro and in vivo. *FEBS Lett* 1993;323:141–144.

Fully Automated Establishment of Stereotaxic Image Orientation in Six Degrees of Freedom for Technetium-99m-ECD Brain SPECT

Jeffrey Tsao, Audrius Stundzia and Masanori Ichise
Department of Nuclear Medicine, Mount Sinai Hospital, and University of Toronto, Toronto, Ontario, Canada

Anatomical localization requires establishing an anatomical space within the image matrix. We developed a fast, fully automated method to establish the image orientation for ^{99m}Tc-ethylcysteinate dimer (ECD) brain SPECT images. **Methods:** The image orientation of ECD brain SPECT images was established in four stages. First, the brain surface was edge-detected as an isosurface at an adaptive threshold. Second, a "convex hull" was determined for the isosurface to minimize regional variability in brain shape. A principal axis transformation and a symmetry vector analysis were applied to the convex hull to resolve the craniocaudal direction and to estimate the midsagittal plane. Third, the brain orientation was refined from this estimate by location of the interhemispheric fissure, the tentorial groove and the frontotemporal groove on the isosurface. Last, the intercommissural (anterior commissure–posterior commissure, or AC–PC) line was detected on the midsagittal slice, and the Talairach grid was scaled to fit the maximal brain dimensions from the AC–PC line. **Results:** The average absolute errors were 2.3° ± 1.5° and 1.08 mm ± 1.11 mm for the midsagittal plane (n = 24) and 2.04° ± 0.80°, 2.0% ± 1.8% of the brain length and 2.3% ± 2.2% of the brain height for the AC–PC line (n = 8). In addition, this program successfully established the image orientation in 94 of 100 clinical ECD brain SPECT studies. Processing time was <40 sec for 128 × 128 × 50 matrices on a DEC Alpha workstation. **Conclusion:** We have developed a fast, robust and fully automated method that determines the orientation of ECD brain SPECT images. This objective method of standardizing the image orientation should be useful for anatomical localization and clinical interpretation of these images.

Key Words: technetium-99m-ECD; brain SPECT; image orientation; automation; image processing

J Nucl Med 1998; 39:503–508

In recent years, there has been increasing recognition of the clinical application of functional brain imaging using SPECT and PET. In interpreting these images, it is often essential to accurately localize detected functional signals in the anatomical space of the brain. This anatomical localization requires establishing an anatomical space within the image matrix. The spatial relationship between the anatomical space and the image matrix is referred to as the image orientation, and it is defined by six degrees of freedom (three translational coordinates along and three rotational angles around the x-, y- and z-axes). A common approach to anatomical localization has been the concurrent use of morphological imaging such as MRI or x-ray CT, which provides detailed anatomical information that functional images may lack (*1–4*). Image coregistration between the two types of imaging modalities allows the image orientation of SPECT or PET to be established in the anatomical space of MRI or CT.

Alternatively, anatomical localization can be achieved by establishing a standard anatomical space, such as the Talairach stereotaxic coordinate system (*5*), in the functional image. An advantage of this approach is that MRI or CT is not required. Furthermore, this approach enables intersubject comparison of corresponding functional signals by matching signals associated with the same stereotaxic locations. In several reports (*6–8*), a standard anatomical space has been established by using fiducial markers for the canthomeatal or orbitomeatal lines to estimate the stereotaxic baseline that passes through the anterior and posterior commissures of the brain (the AC–PC line). However, the limitation of this and other fiducial marker-based methods is the significant variability between the external and the true brain orientations (*9*). An alternative method is to derive information about image orientation, such as the AC–PC line, retrospectively from internal landmarks within the functional image (*10–12*).

In this study, we have developed and evaluated a program that establishes the image orientation for ^{99m}Tc-ethylcysteinate dimer (ECD) brain SPECT images using retrospective image analysis. It uses a combination of new and existing (11,13) image analysis techniques to constrain the image orientation in an incremental fashion. Using a priori knowledge of the characteristic geometry and surface features of the brain, this program can establish the image orientation in a fast and fully automated manner, regardless of the initial image orientation.

MATERIALS AND METHODS

Theory and Algorithms

SPECT brain images were analyzed in four stages to establish the image orientation in six degrees of freedom from the brain geometry:

1. A convex model of the brain surface was created to provide an estimate of the overall brain shape;
2. The brain orientation was estimated from the voxel distribution within the model by using a combination of two analytic techniques: principal axis transformation (PAX) and symmetry vector analysis (SVA);
3. The brain orientation was refined by detection of geometric features of the brain surface to locate the midsagittal and tentorial planes; and
4. The intercommissural (AC–PC) line was located on the midsagittal plane, and the Talairach grid was fitted onto the brain according to the established orientation.

Convex Brain Model. The image voxels were binarized by an adaptive intensity threshold (i.e., 1 = above threshold and 0 = below threshold). The collection of edge voxels above the threshold formed the brain surface. The threshold was defined according to a procedure developed in a preliminary analysis of the ECD SPECT intensity histograms of 14 control subjects and 18 patients. In that analysis, a histogram height representing a volume of 250 mm^3 from the high-intensity side was found to correspond consistently to a relative intensity of 94.9% ± 1.5%. Thus, the intensity value at this point was used as a calibration reference, and the threshold was extrapolated at 35%.

The brain surface exhibited considerable intersubject variation in regional shape. Local concavities and convexities were caused by pathological lesions and increased uptake in surrounding soft tissue, respectively. Local convexities were often small and insignificant. Local concavities (e.g., stroke lesion), on the other hand, were sometimes large and could substantially affect the orientation estimates of PAX (14–16) and SVA used in the subsequent step. Thus, the effects of these variations were minimized by transforming the brain surface into a "convex hull" (17), defined as the smallest polyhedron that could encase the surface. The convex hull masked the local concavities and convexities but preserved the overall geometry. To maximize computational performance, the three-dimensional convex hull was determined by processing individual xy, xz and yz slices separately (but sequentially) along the image matrix axes. On each slice, a convex outline of the brain surface was determined, and the interior of the outline was filled with a uniform intensity to eliminate subcortical variations. The filled-in polygons were then stacked back into a three-dimensional volume, which was subsequently processed along a new slice direction. The final hull had the oblong shape of an ellipsoid flattened on the underside showing an uneven mass distribution with distinctive craniocaudal and anteroposterior directionality (Fig. 1).

Analytic Techniques. The general brain orientation was estimated from the mass distribution of the convex hull using a

combination of PAX and SVA. Principal axis transformation is a well-established technique (13,14,16) that determines three principal axes of mass distribution. Of the three, only the axis with the largest mass distribution was used in this study because its orientation was most stable against variations in brain shape. This principal axis was laid approximately along the anteroposterior axis and was used subsequently to estimate the midsagittal plane (Fig. 2). The two directions of this axis (i.e., anterior and posterior) were indistinguishable in PAX (15), resulting in an anteroposterior ambiguity for the brain orientation. This ambiguity was resolved by detecting the tentorial groove on the posterior surface of the brain.

Symmetry vector analysis is a new technique developed here to estimate the craniocaudal orientation from the average direction of mass distribution around the center of mass, according to the equation:

$$\vec{v}_{Sym} = \sum \hat{v}, \qquad \text{Eq. 1}$$

where $\vec{v}_{Sym}$ is the symmetry vector and $\hat{v}$ is a unit vector pointing from the center of mass to each voxel within the convex hull. Due to the ellipsoidal shape of the convex hull, summation of these unit vectors resulted in their mutual cancellation in the radial direction. The remaining vector components summed to a symmetry vector that always pointed toward the brain vertex along the caudocranial direction (Fig. 2).

The midsagittal plane was estimated as the plane lying on both the principal axis and the symmetry vector. The brain-relative coordinate system was initially defined as follows: the y-axis, the yz plane and the origin were defined as the principal axis, the midsagittal plane and the brain's center of mass, respectively. This brain-relative coordinate system had to be refined subsequently because the estimated midsagittal plane could err up to ±30°.

Orientation Refinement. The brain-relative coordinate system was refined by aligning its coordinate planes with several landmarks located on the unfilled brain surface (i.e., not the surface of the convex hull). These surface landmarks were the interhemispheric fissure, which defined the midsagittal yz plane, and the tentorial and the frontotemporal grooves, which defined the xy plane, referred to as the tentorial plane (Fig. 3).

The surface landmarks were located by identifying regions on the brain surface possessing characteristic local curvatures and gradients, as found in a preliminary study with seven controls and 10 patients (Appendix A). Differences in these characteristic values were observed between the tentorial groove and the frontotemporal groove and were used to resolve the anteroposterior ambiguity. For the interhemispheric fissure, the portion of the brain surface matching the characteristic values was confined in addition to subregions thereof with similar surface normals (Appendix B). The midsagittal and tentorial planes were fitted sequentially and separately to the detected surface features using a least squares minimization of the distance between the planes and the corresponding surface features. The fitted tentorial plane was projected to be perpendicular to the midsagittal plane. The new midsagittal and tentorial planes then redefined the coordinate planes of the brain-relative coordinate system.

Establishment of the Anterior Commissure–Posterior Commissure Line. The position of the AC–PC line on the midsagittal slice was determined using the method of Minoshima et al. (11), with minor modifications (Appendix C). Establishment of the AC–PC line corrected for the rotation on the midsagittal plane. The maximal brain dimensions were measured from the AC–PC line in the craniocaudal and lateral directions and along the AC–PC line in the anteroposterior direction by scanning the image matrix to find
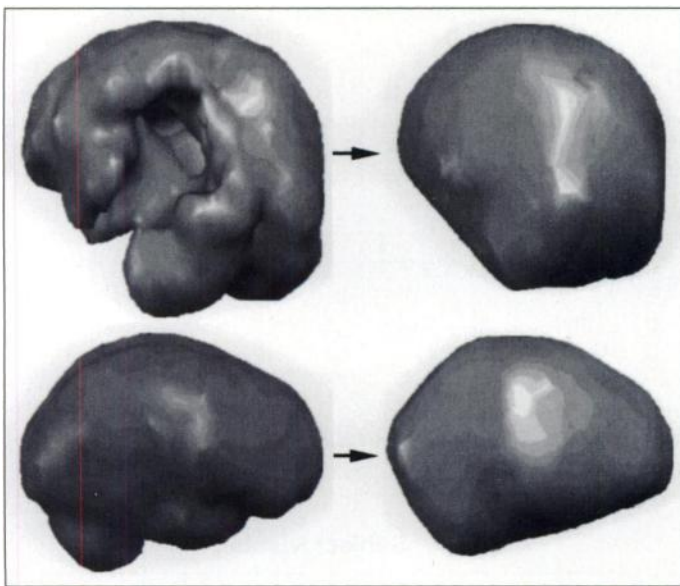
FIGURE 1. Local concavities in the brain shape in both normal (lower left) and pathological (upper left) brains were filled in to create a convex brain surface (right).

FIGURE 2. Typical positions of the principal axis and the symmetry vector, drawn on the unfilled, non-convex brain surface.

the farthest voxels above the 35% intensity threshold. Then, the Talairach grid was scaled to fit these dimensions.

SPECT Studies

ECD brain SPECT images of 10 normal control subjects (6 men and 4 women, ages 23–55 yr) and 14 patients with dementia (8 men and 6 women, ages 40–75 yr) were used for a quantitative validation study, and an additional 100 clinical cases of patients with dementia or traumatic brain injury were used for a semiquantitative evaluation of the present program. The patient group included subjects with a full range of clinical disease severity.

SPECT imaging was performed using a triple-headed system (Prism 3000 XP; Picker International, Inc., Cleveland, OH) equipped with ultra-high-resolution fanbeam collimators and interfaced to a dedicated workstation (Odyssey VP). Each subject received an intravenous injection of 740 MBq (20 mCi) of ECD. Scans were acquired 30 min postinjection for 15 min. For each scan, 120 25-sec projection images were obtained using 3° angle intervals on a 128×128 matrix over 360° by rotating each head 120°. The radius of rotation was fixed at 13.5 cm. Using a Jaszczak phantom (model 7000; Data Spectrum Corporation) and capillary ^{99m}Tc line sources, FWHM was 9.0 mm in water at the center of the field of view. SPECT images were reconstructed using a three-dimensional Butterworth postreconstruction filter (order = 6 and cutoff frequency = 0.30) after applying a ramp back-projection filter. Image voxel dimensions were 2.78 mm $\times$ 2.78 mm $\times$ 3.56 mm. Attenuation correction was performed by assuming uniform attenuation (18) ($\mu = 0.09$ cm^{-1}).

Validation

The quantitative validation study was divided into two phases. The first determined the error in the midsagittal plane. The second determined the error in the AC–PC line on the midsagittal slice. In the first phase, four imaging experts were asked to place 20 digital markers on the midsagittal line of axial images for 10 normal and 14 pathological subjects. The midsagittal plane was determined from the marker positions by regression using a least squares minimization of the marker-to-plane distance. The best-fit plane was compared with the automatically determined plane. The rotational deviation was measured as the absolute angular difference between the plane normals. The translational deviation was
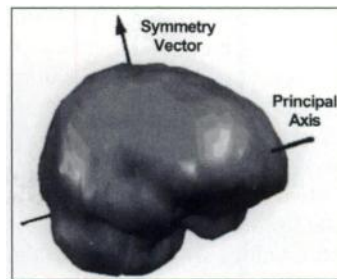
measured at the brain center as the interplane distance along the normal of the automatically determined plane. In the second phase, the true AC–PC line was determined manually on magnetic resonance images and compared to the automatically determined AC–PC line on the SPECT images of the same subjects. This verification was performed for eight of the above subjects, who had both the MRI and SPECT scans taken within 1 mo. Using the method described previously (11), angular difference between the true and automatically determined AC–PC line and horizontal and vertical displacements of the centers of the two lines were measured on coregistered MRI-SPECT images. The coregistration was performed manually by aligning four landmarks: the frontal pole, the inferior aspect of the anterior corpus callosum (CC), the subthalamic point and the occipital pole point. The definitions of these landmarks were described previously (11).

In addition, the present program was evaluated in 100 clinical cases. Images were reformatted according to the determined orientation in axial, coronal and sagittal views with an overlay of the Talairach grid. The images were assessed visually by nuclear medicine experts and classified as failures if the misalignment exceeded 5° in any direction.

RESULTS

Validation

In the quantitative validation study, the present program was successful in determining the orientation for 23 of 24 subjects (10 normal subjects and 14 patients). The remaining subject (Patient 21 in Fig. 4) was problematic for the program due to excessive corrugation on the brain surface resulting from filtering artifacts. Figure 4 shows the mean absolute rotational and translational differences between manually and automatically determined midsagittal planes for all 24 subjects. The data point for each subject was averaged from four evaluators, with the error bars indicating the interevaluator variation. The absolute mean rotational and translational errors for the 23 subjects, excluding the one for which the program failed to
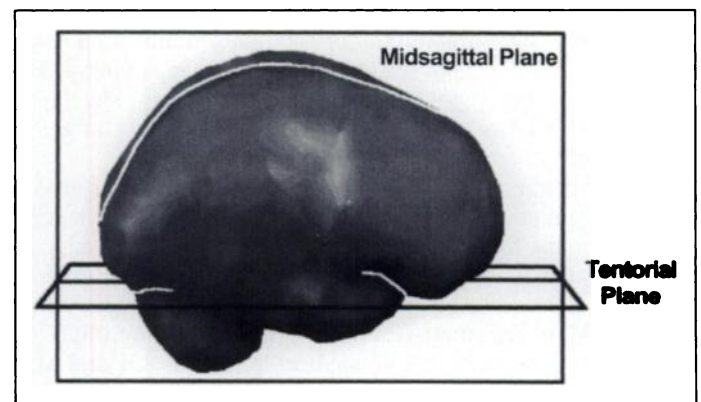

FIGURE 3. The midsagittal and tentorial planes were determined by regression of the marked surface features. The two planes establish the yz and xy planes of the brain-relative coordinate system, respectively.

establish the orientation, were 2.3° ± 1.5° (mean ± s.d.) and 1.08 mm ± 1.11 mm, respectively. For the eight subjects with SPECT and MRI scans, the mean absolute ± s.d. and mean ± s.d. differences between the manually and automatically determined AC–PC line were 2.04° ± 0.80° and −0.09° ± 2.32°, respectively. The mean absolute horizontal and vertical displacements between centers of the two lines were 2.0% ± 1.8% of the anteroposterior length of the brain and 2.3% ± 2.2% of the brain height, respectively. These values were similar to the original results of Minoshima et al. (11).

In the 100 clinical cases, the program established the image orientation correctly according to visual inspection for 94%. Figure 5 shows a typical overlay of the Talairach grid on the reoriented SPECT images. We reran the program on the six problem cases using an increased intensity threshold at 40% or 45%, and the program corrected the image orientation in three cases. In the remaining cases, one subject had a brain that was almost circular in shape when viewed craniocaudally, so PAX was unable to locate the anteroposterior axis. In another, the soft tissue activity was unusually high, so the brain could not be segmented by thresholding. In the third, the AC–PC line could not be determined. The AC–PC line was found in general to be variable in its position, but the variation was small enough (±5°) to be acceptable clinically. In some of the cases, the midsagittal plane was found to be nonplanar. When the midsagittal plane was fitted to the interhemispheric fissure at the cortical region, it deviated from the midsagittal position in the deep structure by up to 4 mm.

Performance Analysis

The method took 22–40 sec to establish the Talairach proportional coordinate system for an image matrix of 128 × 128 × 48 (voxel size 2.84 mm × 2.84 mm × 3.56 mm) on a DEC Alpha 166-MHz AXP workstation. Variations in processing time depended on the number of mass-containing voxels (i.e., the brain size), as well as the number of iterations in plane fitting. To approximate the processing time for larger image matrices, the processing time was plotted against the number of mass-containing voxels in logarithmic-logarithmic scale. The processing time was found to increase at a slower rate than did the square root of the number of voxels.

DISCUSSION

We have presented a fast and fully automated method for orienting ECD brain SPECT images in six degrees of freedom. This method requires neither special acquisition protocols nor operator intervention to constrain the image orientation. It uses a collection of image analysis techniques, each of which analyzes a different aspect of the brain geometry and obtains complementary information for orientation determination based on a priori knowledge of the characteristic brain geometry. The method does not rely on an explicit template of the target structure (19,20), so it allows for greater variability in actual brain shape.

We chose the interhemispheric fissure, the tentorial groove and the frontotemporal groove as appropriate surface features for refining the final brain orientation because they proved to be reliable landmarks that uniquely determined the brain orientation and are clearly visible in normal and most pathological subjects. Moreover, these features are not specific to SPECT, so the current method should be applicable to PET, CT and MRI brain images as well. We did not use features of the subcortical brain structures because these structures exhibited more variability in pathological conditions than did surface features. We found that our prominent surface features were generally
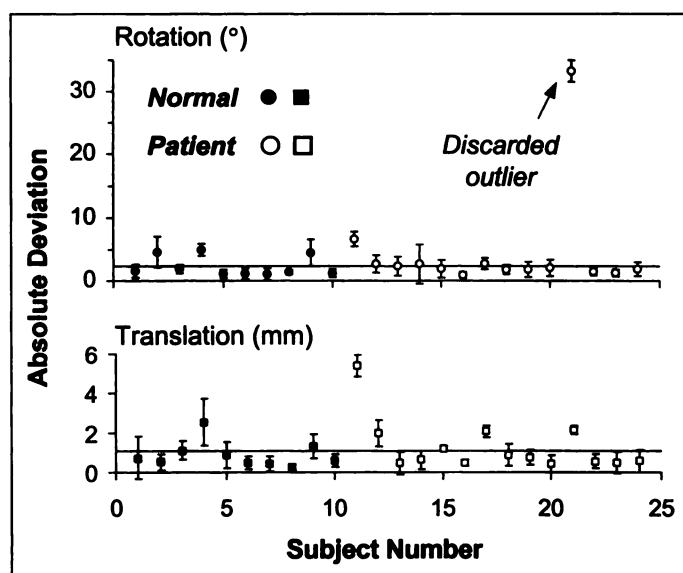

FIGURE 4. The mean absolute difference between the automated and manual determination of the midsagittal plane. Rotational (upper) and translational (lower) differences, respectively. The error bar indicates interevaluator variation. The horizontal line represents the mean difference for all subjects excluding the labeled outlier.

sufficient for accurate orientation determination, as shown by the small differences between manually and automatically determined orientations.

Occasionally, the program encountered problematic cases. In some subjects, the midsagittal plane was significantly nonplanar. Therefore, the midsagittal plane, being estimated from the cortical region, poorly approximated the midsagittal position around the thalamus. In other subjects, the interhemispheric fissure was not prominent on brain surface due to extra surface corrugations introduced by lesions, increased soft tissue activity and/or improper sinusoidal filter settings. In these cases, the program was unable to locate the interhemispheric fissure, but the problem was often corrected after increasing the intensity threshold. In contrast, the tentorial and frontotemporal grooves were usually more prominent, and the program did not have difficulties in locating them. Similar threshold adjustments may be needed for applying the current program to HMPAO, which is known to have increased soft tissue uptake. Perhaps in the future, problems with surface feature delineation can be overcome by using surfaces at multiple intensity thresholds. Surface features found on one surface can be used to locate corresponding features on other surfaces. Only those features consistently found on several surfaces are considered the correctly identified ones. However, the processing time also will increase approximately linearly with the number of surfaces used. Currently, the processing time of 22–40 sec is fast due to the use of surface features. Voxels pertaining to the surface features only constituted a minor proportion of all image voxels, so the computational load for the current method was relatively light.

In our method, we incorporated a modified version of the Minoshima's algorithm (11) to determine the AC–PC line. This line was needed to reorient the brain-relative coordinate system established by PAX, SVA and surface feature detection along with the Talairach proportional coordinate system. Although the former coordinate system was already sufficient for coregistering SPECT, PET, CT or MRI image of the same subject, it was insufficient for anatomical localization because it had considerable rotational variations between subjects in relation to the Talairach proportional coordinate system, depending on the relative positions of the cerebrum and the tentorial groove.
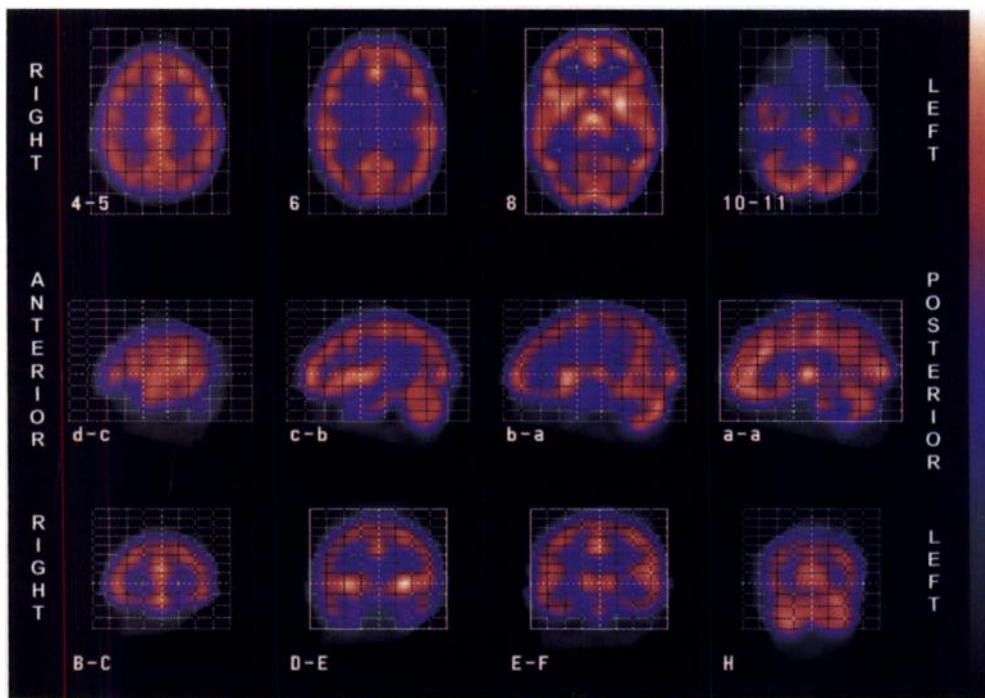
FIGURE 5. Selected transverse (upper), sagittal (right hemisphere, middle) and coronal (lower) tomographic images of ^{99m}Tc-ECD brain of a 32-yr-old healthy woman. Each image is indicated by number(s), letter(s) or their combinations, which correspond to those found in the Talairach stereotaxic atlas (*1*).

The AC–PC line was, therefore, needed for anatomical localization. The method of Minoshima et al. (*11*), which was originally developed for [^{18}F]fluorodeoxyglucose PET was, however, somewhat vulnerable to intersubject variations for our ECD SPECT images for two main reasons. Identification of the CC was pivotal in the algorithm because the rest of the landmarks depended on the correct identification of this initial landmark. However, the contour-finding algorithm that determined the approximate CC was vulnerable to the extraneous contours introduced by pathological lesions. This problem was rectified in our implementation, as described in Appendix C. In addition, as discussed by Minoshima et al. (*11*), the four landmarks needed to define the AC–PC line were sometimes unavailable in certain pathological cases (e.g., Pick's disease and stroke). The use of additional landmarks may cope with these situations in the future.

We have applied this method, without the AC–PC determination, successfully to images of other modalities (PET and MRI) as well (*unpublished data*). PET images required no modifications to the existing algorithms. For MRI images, we first applied an intensity-based method to remove the scalp from MRI T2-weighted images. Then, we applied the current method to the segmented MRI images. The threshold for delineating the brain surface was modified to suit the MRI intensities. After establishing the image orientation, we were able to coregister the corresponding SPECT and PET or SPECT and MRI images by overlapping the corresponding axes of the brain-relative coordinate system. The coregistration showed good results, with estimated errors of 2 mm, and the entire processing time, including the segmentation, was ~1 min.

CONCLUSION

We have developed a fast, robust and fully automated method that establishes the anatomical orientation for ECD brain SPECT images by using a priori knowledge of the brain geometry. This program should facilitate interpretation of clinical ECD brain SPECT images by providing an objective method for anatomical localization.

APPENDIX A

Assessment of Local Curvature and Gradient

The interhemispheric fissure was located by examining the brain surface from eight angles (0°, 20°, 45°, 75°, 105°, 135°, 160° and 180°). The tentorial and frontotemporal grooves were located by examination from two angles (190° and 350°). These angles specify rotation on the midsagittal plane around the brain center relative to the principal axis, which defined 0° and 180°. Due to the anteroposterior ambiguity, 0° could refer to either the anterior or posterior side. This ambiguity was resolved during subsequent detection of the tentorial fissure at one of the two angles above. The 0°–180° and 180°–360° ranges refer to the superior and inferior sides of the brain surface, respectively.

At each angle, the brain surface was obtained by detecting the outermost isoactive surface at the 35% threshold using ray casting (Fig. 6). The detected surface points were represented collectively as an elevation map on a rectangular grid (z-buffer). Neighboring points on the elevation map were either fitted to a parabola (for the interhemispheric fissure) or joined together by vectors (for the tentorial and frontotemporal grooves). The parabolic parameters or the vector directions measured the local curvature and gradient and were compared with the predetermined values for the surface features. Each surface feature (i.e., the interhemispheric fissure and the tentorial or frontotemporal groove) was then defined as the collection of points matching its predetermined characteristic values for the local curvature and gradient.
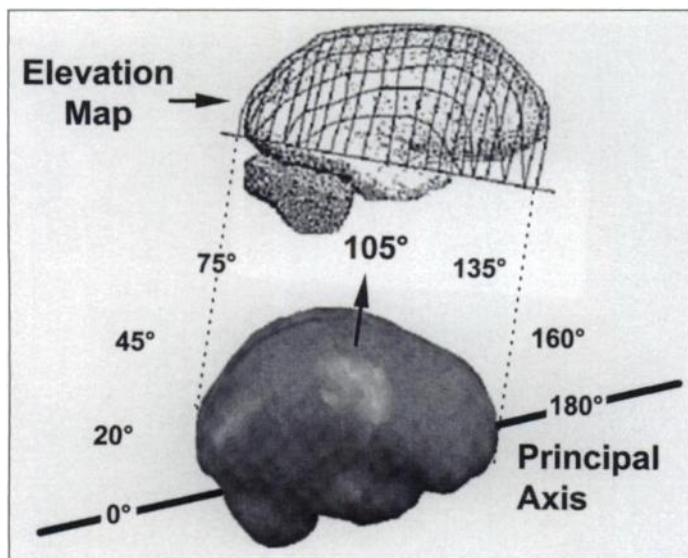
FIGURE 6. Illustration of an elevation map created at 105° by ray casting. The angles are specified relative to the principal axis, which defines 0° and 180°. In this particular case, 0° defines the posterior side.

APPENDIX B

Localization of the Interhemispheric Fissure

The elevation maps from the eight examination angles were processed separately. On each elevation map, we first selected all the points matching the characteristic local curvature and gradient. Then, the selected points were projected along the height axis of the elevation map onto the convex hull. At each projected point, the angle of the "two-dimensional surface normal" was measured as described below. The distribution of angles was determined, and points associated with outlying angles (i.e., farthest from the mean) were removed iteratively until a predefined criterion was met. The criterion was established empirically to evaluate the following function:

$$s.d./n^{1.5}, \qquad \text{Eq. 2}$$

where s.d. = s.d. of the angles and n = number of remaining positions. The iteration ended when this function reached the local minimum before the global maximum. The collection of remaining points specified the location of the interhemispheric fissure. This procedure was repeated separately for the elevation map of every angle.

To determine the angle of the two-dimensional surface normal, the convex hull was divided into parallel strips that ran along the left → right direction. Only those strips that contained projected points were examined. Each strip was a two-dimensional cross-sectional graph of the convex hull, with the x and y axes running along the strip direction and the height axis of the elevation map, respectively. Every projected point on the two-dimensional graph had a normal vector, and the angle between this vector and the y axis was the angle of interest.

APPENDIX C

AC–PC Line Detection

The following modifications were made to the method of Minoshima et al. ([11]):

1. A Butterworth filter was applied before the processing of the images, so it was not applied again for the resampled slices;
2. Edge detection was performed by using intensity thresholding at 45% instead of a combination of a smoothing filter and a Laplacian filter; and
3. Landmarks were located within window areas around expected locations to avoid erroneous detection in other areas with confusing contours that resulted from lesions or soft tissue activity in the nasal area on the SPECT images of some subjects.

REFERENCES

1. Evans AC, Beil C, Thompson CJ, Hakim A. Anatomical–functional correlation using an adjustable MRI-based region of interest atlas with PET. *J Cereb Blood Flow Metab* 1988;8:513–530.
2. Evans AC, Marrett S, Torrescorzo J, Ku S, Collins L. MRI-PET correlation in three dimensions using a volume-of-interest (VOI) atlas. *J Cereb Blood Flow Metab* 1991;11:A69–A78.
3. Ge Y, Fitzpatrick JM, Votaw JR, et al. Retrospective registration of PET and MR brain images: an algorithm and its stereotaxic validation. *J Nucl Med* 1994;18:800–810.
4. Andersson JLR, Sundin A, Valind S. A method for coregistration of PET and MR brain images. *J Nucl Med* 1995;36:1307–1315.
5. Talairach J, Tournoux P, Rayport M, eds. *Co-planar stereotaxic atlas of the human brain. Three-dimensional proportional system: an approach to cerebral imaging.* New York: Thieme Inc.; 1988;1–122.
6. Fox PT, Perlmutter JS, Raichle ME. A stereotactic method of anatomical localization for positron emission tomography. *J Comput Assist Tomogr* 1985;9:141–153.
7. Vanier M, Lecours AR, Ethier R, et al. Proportional localization system for anatomical interpretation of cerebral computed tomograms. *J Comput Assist Tomogr* 1985;9:715–724.
8. Ichise M, Toyoma H, Vines DC, Chung D-G, Kirsh JC. Neuroanatomical localization for clinical SPECT perfusion brain imaging: a practical proportional grid method. *Nucl Med Commun* 1992;13:861–866.
9. Tokunaga A, Takase M, Otani K. The glabella-inion line as a baseline for CT scanning of the brain. *Neuroradiology* 1977;14:67–71.
10. Brummer ME. Hough transform detection of the longitudinal fissure in tomographic head images. *IEEE Trans Med Imaging* 1991;10:74–81.
11. Minoshima S, Koeppe RA, Mintun MA, et al. Automated detection of the intercommissural line for stereotactic localization of functional brain images. *J Nucl Med* 1993;34:322–329.
12. Guimond A, Meunier J, Soucy J-P. Automated detection of the brain intercommissural line from SPECT data. *Proc IEEE-EMBC CMBEC* 1995:453–454.
13. Alpert NM, Brad JF, Kennedy D, Correia JA. The principal axes transformation: a method for image registration. *J Nucl Med* 1990;31:1717–1722.
14. Rusinek H, Tsui WH, Levy AV, Noz ME, de Leon MJ. Principal axes and surface fitting methods for three-dimensional image registration. *J Nucl Med* 1993;34:2019–2024.
15. Toga AW, Banerjee PK. Registration revisited. *J Neurosci Methods* 1993;48:1–13.
16. Weber DA, Ivanovic M. Correlative image registration. *Semin Nucl Med* 1994;24:311–323.
17. Nyström I, Bengtsson E, Nordin B, Borgefors G. Quantitative analysis of volume images: electron microscopic tomography of HIV. *Proc SPIE Image Processing* 1994;2167:296–303.
18. Chang L. A method for attenuation correction in radionuclide computed tomography. *IEEE Trans Nucl Sci* 1978;NS-25:638–643.
19. Bajcsy R, Lieberson R, Reivich M. A computerized system for the elastic matching of deformed radiographic images to idealized atlas images. *J Comput Assist Tomogr* 1983;7:618–625.
20. Slomka PJ, Hurwitz GA, Stephenson J, Cradduck T. Automated alignment and sizing of myocardial stress and rest scans to three-dimensional normal templates using an image registration algorithm. *J Nucl Med* 1995;36:1115–1122.